

# Grain Growth and the Effect of Different Time Scales

Katayun Barmak, Anastasia Dunca, Yekaterina Epshteyn, Chun Liu and Masashi Mizuno

**Abstract:** Many technologically useful materials are polycrystals composed of a myriad of small monocrystalline grains separated by grain boundaries. Dynamics of grain boundaries play a crucial role in determining the grain structure and defining the materials properties across multiple scales. In this work, we consider two models for the motion of grain boundaries with the dynamic lattice misorientations and the triple junctions drag, and we conduct extensive numerical study of the models, as well as present relevant experimental results of grain growth in thin films.

**Key words:** Grain growth, grain boundary network, texture development, lattice misorientation, triple junction drag, energetic variational approach, geometric evolution equations, thin films, Grain Boundary Character Distribution (GBCD)

**AMS:** 74N15; 35R37; 53C44; 49Q20

## 1 Introduction

Many technologically useful materials are polycrystals composed of a myriad of small monocrystalline grains separated by grain boundaries, see Figures 1-2. Dy-

---

Katayun Barmak

Columbia University, New York, NY 10027, USA, e-mail: kb2612@columbia.edu

Anastasia Dunca

West High School, Salt Lake City, UT 84103, USA, e-mail: anastasia.d960@slcstudents.org

Yekaterina Epshteyn

University of Utah, Salt Lake City, UT 84112, USA, e-mail: epshteyn@math.utah.edu

Chun Liu

Illinois Institute of Technology, Chicago, IL 60616, USA, e-mail: cliu124@iit.edu

Masashi Mizuno

Nihon University, Tokyo 101-8308 JAPAN, e-mail: mizuno@math.cst.nihon-u.ac.jp

namics of grain boundaries play a crucial role in determining the grain structure and defining materials properties across multiple scales. Experimental and computational studies give useful insight into the geometric features and the crystallography of the grain boundary network in polycrystalline microstructures.

In this work, we consider two models for the motion of grain boundaries in a planar network with dynamic lattice misorientations and with drag of triple junctions. A classical model for the motion of grain boundaries in polycrystalline materials is growth by curvature, as a local evolution law for the grain boundaries due to Mullins and Herring [17, 28, 29], and see work on mean curvature flow, e.g., [11, 12, 15, 25, 23]. In addition, to have a well-posed model for the evolution of the grain boundary network, one has to impose a separate condition at the triple junctions where three grain boundaries meet [20]. A conventional choice is the Herring condition which is the natural boundary condition at the triple points for the grain boundary network at equilibrium, [9, 10, 20, 18], and reference therein. There are several studies about grain boundary motion by mean curvature with the Herring condition at the triple junctions, see for instance [20, 26, 6, 5, 8, 4, 22, 7, 1, 16, 21, 37].

A standard assumption in the theory and simulations of grain growth is to address only the evolution of the grain boundaries/interfaces themselves and not the dynamics of the triple junctions. However, recent experimental work indicates that the motion of the triple junctions together with the anisotropy of the grain interfaces can have a significant effect on the resulting grain growth [7], see work on molecular dynamics simulation [37, 36], a recent work on dynamics of line defects [38, 39, 34] and a relevant work on numerical analysis of a vertex model [35]. The current work is a continuation of our previous work [14, 13], where we proposed a new model for the evolution of planar grain boundaries, which takes into account dynamic lattice misorientations (evolving anisotropy of grain boundaries or “grains rotations”) and the mobility of the triple junctions. In [14, 13], using the energetic variational approach, we derived a system of geometric differential equations to describe the motion of such grain boundaries, and we established a local well-posedness result, as well as large time asymptotic behavior for the model. In addition, in [13], similar to our previous work on Grain Boundary Character Distribution, e.g. [5, 4] we conducted some numerical experiments for the 2D grain boundary network in order to illustrate the effect of time scales, e.g. of the mobility of triple junctions and of the dynamics of misorientations on how the grain boundary system decays energy and coarsens with time (note, in [13], we studied numerically only the model with curved grain boundaries). Our current goal is to conduct extensive numerical studies of two models, a model with curved grain boundaries and a model without curvature/“vertex model” of planar grain boundaries network with the dynamic lattice misorientations and with the drag of triple junctions [14, 13] and to further understand the effect of relaxation time scales, e.g. of the curvature of grain boundaries, mobility of triple junctions and dynamics of misorientations on how the grain boundary system decays energy and coarsens with time. We also present and discuss relevant experimental results of grain growth in thin films.

The paper is organized as follows. In Sections 2-3, we discuss and review important details and properties of the two models for grain boundary motion. In

Sections 4.1, we present and discuss relevant experimental findings of grain growth in thin films, and in Section 4.2 we conduct extensive numerical studies of the grain growth models.

## 2 Review of the Models with Single Triple Junction

In this paper we use recently developed models for the evolution of the planar grain boundary network with dynamic lattice misorientations and triple junction drag [14, 13] to study the effect of time scales of curvature of grain boundaries, dynamics of the triple junctions and dynamics of the misorientations on grain growth. Thus, in this section for the reader's convenience, we first review the models which were originally developed in [14, 13].

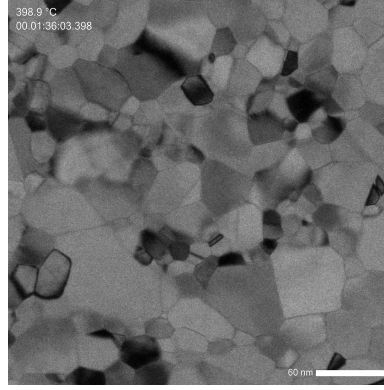


**Fig. 1** Experimental microstructure: drift-corrected bright-field image of a 50 nm-thick Pt film from an instance of the in-situ grain growth experiment in the transmission electron microscope.

Let us first recall the system for a single triple junction which was derived in [14]. The total grain boundary energy for such model is

$$\sum_{j=1}^3 \sigma(\Delta^{(j)}\alpha) |\Gamma_t^{(j)}|. \quad (1)$$

Here,  $\sigma : \mathbb{R} \rightarrow \mathbb{R}$  is a given surface tension,  $\alpha^{(j)} = \alpha^{(j)}(t) : [0, \infty) \rightarrow \mathbb{R}$  is time-dependent orientations of the grains,  $\theta = \Delta^{(j)}\alpha := \alpha^{(j-1)} - \alpha^{(j)}$  is a lattice misorientation of the grain boundary  $\Gamma_t^{(j)}$  (difference in the orientation between two neighboring grains that share the grain boundary), and  $|\Gamma_t^{(j)}|$  is the length of  $\Gamma_t^{(j)}$ . As a result of applying the maximal dissipation principle, in [14], the following model was derived,

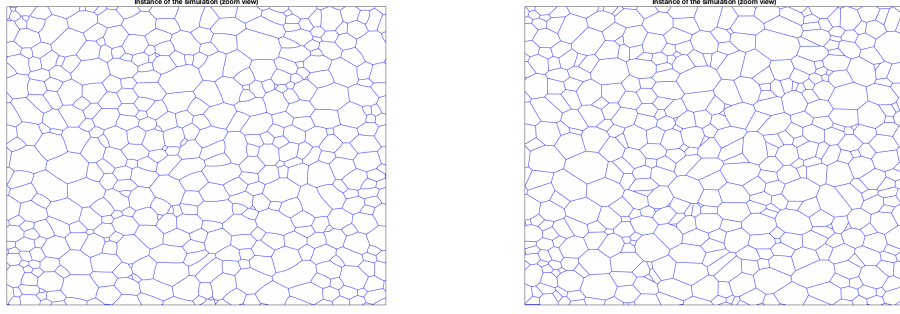


**Fig. 2** Left figure - microstructure from simulation, model with curvature and finite mobility of the triple junctions (2): example of a time instance during the simulated evolution of a cellular network (zoom view). Right figure - microstructure from simulation, model without curvature (3): example of a time instance during the simulated evolution of a cellular network (zoom view).

$$\begin{cases}
 v_n^{(j)} = \mu \sigma(\Delta^{(j)} \alpha) \kappa^{(j)}, & \text{on } \Gamma_t^{(j)}, t > 0, \quad j = 1, 2, 3, \\
 \frac{d\alpha^{(j)}}{dt} = -\gamma \left( \sigma_\theta(\Delta^{(j+1)} \alpha) |\Gamma_t^{(j+1)}| - \sigma_\theta(\Delta^{(j)} \alpha) |\Gamma_t^{(j)}| \right), & j = 1, 2, 3, \\
 \frac{d\mathbf{a}}{dt}(t) = \eta \sum_{k=1}^3 \sigma(\Delta^{(k)} \alpha) \frac{\mathbf{b}^{(k)}(0, t)}{|\mathbf{b}^{(k)}(0, t)|}, & t > 0, \\
 \Gamma_t^{(j)} : \xi^{(j)}(s, t), & 0 \leq s \leq 1, \quad t > 0, \quad j = 1, 2, 3, \\
 \mathbf{a}(t) = \xi^{(1)}(0, t) = \xi^{(2)}(0, t) = \xi^{(3)}(0, t), & \text{and } \xi^{(j)}(1, t) = \mathbf{x}^{(j)}, \quad j = 1, 2, 3.
 \end{cases} \quad (2)$$

In (2),  $v_n^{(j)}$ ,  $\kappa^{(j)}$ , and  $\mathbf{b}^{(j)} = \xi_s^{(j)}$  are a normal velocity, a curvature and a tangent vector of the grain boundary  $\Gamma_t^{(j)}$ , respectively. Note that  $s$  is not an arc length parameter of  $\Gamma_t^{(j)}$ , namely,  $\mathbf{b}^{(j)}$  is *not* necessarily a unit tangent vector. The vector  $\mathbf{a} = \mathbf{a}(t) : [0, \infty) \rightarrow \mathbb{R}^2$  defines a position of the triple junction (triple junctions are where three grain boundaries meet),  $\mathbf{x}^{(j)}$  is a position of the end point of the grain boundary. The three independent relaxation time scales  $\mu, \gamma, \eta > 0$  (curvature, misorientation and triple junction dynamics) are regarded as positive constants. Further, we assume in (2),  $\alpha^{(0)} = \alpha^{(3)}$ ,  $\alpha^{(4)} = \alpha^{(1)}$  and  $\mathbf{b}^{(4)} = \mathbf{b}^{(1)}$ , for simplicity. We also use notation  $|\cdot|$  for a standard euclidean vector norm. The complete details about model (2) can be found in the earlier work [14, Section 2]. Next, in [14], the curvature effect was relaxed, by taking the limit  $\mu \rightarrow \infty$ , and the reduced model without curvature was derived,

$$\begin{cases} \frac{d\alpha^{(j)}}{dt} = -\gamma \left( \sigma_\theta(\Delta^{(j+1)}\alpha) |\mathbf{b}^{(j+1)}| - \sigma_\theta(\Delta^{(j)}\alpha) |\mathbf{b}^{(j)}| \right), & j = 1, 2, 3, \\ \frac{d\mathbf{a}}{dt}(t) = \eta \sum_{j=1}^3 \sigma(\Delta^{(j)}\alpha) \frac{\mathbf{b}^{(j)}}{|\mathbf{b}^{(j)}|}, & t > 0, \\ \mathbf{a}(t) + \mathbf{b}^{(j)}(t) = \mathbf{x}^{(j)}, & j = 1, 2, 3. \end{cases} \quad (3)$$

In (3), we consider  $\mathbf{b}^{(j)}(t)$  as a grain boundary. Note that, similar to (2), the system of equations (3) can also be derived from the energetic variational principle for the total grain boundary energy (1) (with  $|\Gamma_t^{(j)}|$  replaced by  $|\mathbf{b}^{(j)}|$ ).

*Remark 1 a)* As was discussed in [14], the reduced model without curvature effect (3) is not a standard ODE system. This is the ODE system where each variable is locally constrained. Moreover, local well-posedness result (e.g. local existence result) for the original model (2) will not imply local well-posedness result for the reduced system (3). It is not known if the reduced model (3) is a small perturbation of (2).

**b)** The reduced model (3) captures the dynamics of the orientations /misorientations and the triple junctions. At the same time, it was more accessible for the mathematical analysis than the model (2). In addition, the system (3) is a generalization to higher dimension and dynamic misorientations of the model from [5, 8]. In this paper, we will compare and contrast through extensive numerical studies the model with the curvature effect (2) and the reduced model (3).

To establish local well-posedness result for model (3) in [14], the surface tension  $\sigma$  was assumed to be  $C^3$ , positive, and minimized at 0, namely,

$$\sigma(\theta) \geq \sigma(0) > 0, \quad (4)$$

for  $\theta \in \mathbb{R}$ . In addition, it was assumed convexity of  $\sigma(\theta)$ , for all  $\theta \in \mathbb{R}$ ,

$$\sigma_\theta(\theta)\theta \geq 0, \quad \text{and} \quad \sigma_{\theta\theta}(0) > 0, \quad (5)$$

and

$$\sigma_\theta(\theta) = 0 \text{ if and only if } \theta = 0. \quad (6)$$

Let us review some of the important theoretical results established for (3) in previous work [14, 13]. First, consider the equilibrium state of the system (3), namely,

$$\begin{cases} 0 = - \left( \sigma_\theta(\Delta^{(j+1)}\alpha_\infty) |\mathbf{b}_\infty^{(j+1)}| - \sigma_\theta(\Delta^{(j)}\alpha_\infty) |\mathbf{b}_\infty^{(j)}| \right), & j = 1, 2, 3, \\ \mathbf{0} = \sum_{j=1}^3 \sigma(\Delta^{(j)}\alpha_\infty) \frac{\mathbf{b}_\infty^{(j)}}{|\mathbf{b}_\infty^{(j)}|}, \\ \mathbf{a}_\infty = \mathbf{x}^{(1)} - \mathbf{b}_\infty^{(1)} = \mathbf{x}^{(2)} - \mathbf{b}_\infty^{(2)} = \mathbf{x}^{(3)} - \mathbf{b}_\infty^{(3)}. \end{cases} \quad (7)$$

As in [14, 13], assume, for each  $i = 1, 2, 3$ ,

$$\left| \sum_{j=1, j \neq i}^3 \frac{\mathbf{x}^{(j)} - \mathbf{x}^{(i)}}{|\mathbf{x}^{(j)} - \mathbf{x}^{(i)}|} \right| > 1. \quad (8)$$

The assumption (8) implies that fixed points  $\mathbf{x}^{(1)}$ ,  $\mathbf{x}^{(2)}$  and  $\mathbf{x}^{(3)}$  can not belong to the single line. Furthermore, (8) is equivalent to the condition that in the triangle with vertices  $\mathbf{x}^{(1)}\mathbf{x}^{(2)}\mathbf{x}^{(3)}$ , all three angles are less than  $\frac{2\pi}{3}$ . Next, from the assumptions (8), (5)-(6), associated equilibrium system (7) becomes,

$$\begin{cases} \sum_{j=1}^3 \frac{\mathbf{b}_{\infty}^{(j)}}{|\mathbf{b}_{\infty}^{(j)}|} = \mathbf{0}, \\ \mathbf{a}_{\infty} + \mathbf{b}_{\infty}^{(j)} = \mathbf{x}^{(j)}, \quad j = 1, 2, 3. \end{cases} \quad (9)$$

In [14], it was shown that the assumptions (5)-(6) imply  $\alpha_{\infty}^{(1)} = \alpha_{\infty}^{(3)} = \alpha_{\infty}^{(3)}$ , hence  $\Delta^{(j)}\alpha_{\infty} = 0$  for  $j = 1, 2, 3$  for the equilibrium system (7) (note, that in this case, for the purpose of mathematical modeling, one can still assume a “fictitious” grain boundary with the same orientation on each side of the grain boundary. In addition, in this work we study the grain boundary system before it reaches a state of constant orientations, see Section 4.)

We also have energy dissipation principle for the system (3),

**Proposition 1 (Energy dissipation[14, Proposition 5.1])**

*Let  $(\alpha, \mathbf{a})$  be a solution of (3) on  $0 \leq t \leq T$ , and let  $E(t)$ , given by (1), be the total grain boundary energy of the system. Then, for all  $0 < t \leq T$ ,*

$$E(t) + \frac{1}{\gamma} \int_0^t \left| \frac{d\alpha}{d\tau}(\tau) \right|^2 d\tau + \frac{1}{\eta} \int_0^t \left| \frac{d\mathbf{a}}{d\tau}(\tau) \right|^2 d\tau = E(0). \quad (10)$$

Next, define, constant as in [13],

$$C_1 := \inf \left\{ \sum_{j=1}^3 |\mathbf{x}^{(j)} - \mathbf{a}| : \text{There exists } j = 1, 2, 3 \text{ such that } |\mathbf{a} - \mathbf{a}_{\infty}| \geq \frac{1}{2} |\mathbf{b}_{\infty}^{(j)}| \right\}. \quad (11)$$

Assume also that an initial data  $(\alpha_0, \mathbf{a}_0)$  satisfies,

$$E(0) = \sum_{j=1}^3 \sigma(\Delta^{(j)}\alpha_0) |\mathbf{a}_0 - \mathbf{x}^{(j)}| < \sigma(0)C_1. \quad (12)$$

Then, one can establish the global existence result for the model (3),

**Theorem 1 (Global existence[13, Theorem 4.1])**

*Let  $\mathbf{x}^{(1)}, \mathbf{x}^{(2)}, \mathbf{x}^{(3)} \in \mathbb{R}^2$ ,  $\mathbf{a}_0 \in \mathbb{R}^2$ , and  $\alpha_0 \in \mathbb{R}^3$  be the initial data for the system (3). Assume (8), and let  $\mathbf{a}_{\infty}$  be a unique solution of the equilibrium system (9). Further, assume condition (12). Then there exists a unique global in time solution  $(\alpha, \mathbf{a})$  of (3).*

We also have the following large time asymptotic behavior results for the solution of system (3),

**Proposition 2 (Large Time Asymptotic[13, Proposition 5.1])**

Let  $\mathbf{x}^{(1)}, \mathbf{x}^{(2)}, \mathbf{x}^{(3)} \in \mathbb{R}^2$ ,  $\mathbf{a}_0 \in \mathbb{R}^2$ , and  $\alpha_0 \in \mathbb{R}^3$  be the initial data for the system (3). We assume that the initial data satisfy (12), and we also impose the same assumptions as in Theorem 1. Define  $\alpha_\infty$  as,

$$\alpha_\infty := \frac{\alpha_0^{(1)} + \alpha_0^{(2)} + \alpha_0^{(3)}}{3}. \quad (13)$$

Let  $\mathbf{a}_\infty$  be a solution of the equilibrium system (9) and  $(\alpha, \mathbf{a})$  be a time global solution of (3). Then,

$$\alpha(t) \rightarrow \alpha_\infty(1, 1, 1), \quad \mathbf{a}(t) \rightarrow \mathbf{a}_\infty, \quad (14)$$

as  $t \rightarrow \infty$ .

**Theorem 2 (Large Time Asymptotic[13, Theorem 5.1])**

There is a small constant  $\varepsilon_1 > 0$  such that, if  $|\alpha_0 - \alpha_\infty| + |\mathbf{a}_0 - \mathbf{a}_\infty| < \varepsilon_1$ , then the associated global solution  $(\alpha, \mathbf{a})$  of the system (3) satisfies,

$$|\alpha(t) - \alpha_\infty| + |\mathbf{a}(t) - \mathbf{a}_\infty| \leq C_2 e^{-\lambda^* t}, \quad (15)$$

for some positive constants  $C_2, \lambda^* > 0$ .

*Remark 2* The decay order  $\lambda^*$  in (15) is explicitly estimated as,

$$\lambda^* \geq \lambda, \quad (16)$$

where  $\lambda$  depends on  $\gamma, \eta, \sigma_{\theta\theta}(0), \sigma(0)$  and on the smallest positive eigenvalues of the linearized operators for the equations of the orientation  $\alpha$  and of the triple junction  $\mathbf{a}$ .

**Corollary 1 (Large Time Asymptotic[13, Corollary 5.1])** Under the same assumption as in Theorem 2, the associated grain boundary energy  $E(t)$  satisfies,

$$E(t) - E_\infty \leq C_3 e^{-\lambda^* t}, \quad (17)$$

for some positive constant  $C_3 > 0$ , where

$$E_\infty := \sigma(0) \sum_{j=1}^3 |\mathbf{b}_\infty^{(j)}|.$$

**Proof** For the reader's convenience, we will review the proof from [13]. Since  $\alpha_\infty^{(1)} = \alpha_\infty^{(2)} = \alpha_\infty^{(3)}$ , we obtain

$$\begin{aligned}
E(t) - E_\infty &= \sum_{j=1}^3 \left( \sigma(\Delta^{(j)}\alpha(t)) |\mathbf{b}^{(j)}(t)| - \sigma(0) |\mathbf{b}_\infty^{(j)}| \right) \\
&\leq \sum_{j=1}^3 \left( \sigma(0) |\mathbf{b}^{(j)}(t) - \mathbf{b}_\infty^{(j)}| + \left( \sigma(\Delta^{(j)}\alpha(t)) - \sigma(0) \right) |\mathbf{b}^{(j)}(t)| \right) \\
&\leq \sum_{j=1}^3 \left( \sigma(0) |\mathbf{a}^{(j)}(t) - \mathbf{a}_\infty| + \left( C_4 |\Delta^{(j)}\alpha(t)| \right) |\mathbf{b}^{(j)}(t)| \right) \\
&\leq \sum_{j=1}^3 \left( \sigma(0) |\mathbf{a}^{(j)}(t) - \mathbf{a}_\infty| + 2C_4 |\mathbf{b}^{(j)}(t)| |\alpha(t) - \alpha_\infty| \right),
\end{aligned} \tag{18}$$

where  $C_4 = \sup_{|\theta| < 2\varepsilon_1} |\sigma_\theta(\theta)|$ . Using the dissipation estimate (10) and the exponential decay estimate (15), we obtain (17).  $\square$

*Remark 3* Note, that the obtained exponential decay to equilibrium, see estimates (15) and (17) was obtained by considering linearized problem, Lemma 5.1 in [13]. Consideration of the model with curvature - with finite  $\mu$ , (2) and of the nonlinear problem instead of linearized problem could lead to potential power laws estimates for the decay rates. See also discussion and numerical studies in Section 4.

### 3 Extension to Grain Boundary Network

In this section, we review the extension of the results to a grain boundary network  $\{\Gamma_t^{(j)}\}$ . As in [14, 13], we define the total grain boundary energy of the network, like,

$$E(t) = \sum_j \sigma(\Delta^{(j)}\alpha) |\Gamma_t^{(j)}|, \tag{19}$$

where  $\Delta^{(j)}\alpha$  is a misorientation, a difference between the lattice orientation of the two neighboring grains which form the grain boundary  $\Gamma_t^{(j)}$ . Then, the energetic variational principle leads to a full model (network model analog of a single triple junction system (2)),

$$\begin{cases} v_n^{(j)} = \mu \sigma(\Delta^{(j)}\alpha) \kappa^{(j)}, & \text{on } \Gamma_t^{(j)}, t > 0, \\ \frac{d\alpha^{(k)}}{dt} = -\gamma \frac{\delta E}{\delta \alpha^{(k)}}, \\ \frac{d\mathbf{a}^{(l)}}{dt} = \eta \sum_{\mathbf{a}^{(l)} \in \Gamma_t^{(j)}} \left( \sigma(\Delta^{(j)}\alpha) \frac{\mathbf{b}^{(j)}}{|\mathbf{b}^{(j)}|} \right), & t > 0. \end{cases} \tag{20}$$

As in [14], we consider the relaxation parameters,  $\mu \rightarrow \infty$ , and we further assume that the energy density  $\sigma(\theta)$  is an even function with respect to the misorientation  $\theta =$



$\Delta^{(j)}\alpha$ , that is, the misorientation effects are symmetric with respect to the difference between the lattice orientations. Then, the problem (20) reduces to (network model analog of a single triple junction system (3) ),

$$\left\{ \begin{array}{l} \Gamma_t^{(j)} \text{ is a line segment between some } \mathbf{a}^{(l_{j,1})} \text{ and } \mathbf{a}^{(l_{j,2})}, \\ \frac{d\alpha^{(k)}}{dt} = -\gamma \sum_{\substack{\text{grain with } \alpha^{(k')} \text{ is the neighbor of the grain with } \alpha^{(k)} \\ \Gamma_t^{(j)} \text{ is formed by the two grains with } \alpha^{(k)} \text{ and } \alpha^{(k')}}} |\Gamma_t^{(j)}| \sigma_\theta(\alpha^{(k)} - \alpha^{(k')}), \\ \frac{d\mathbf{a}^{(l)}}{dt} = \eta \sum_{\mathbf{a}^{(l)} \in \Gamma_t^{(j)}} \left( \sigma(\Delta^{(j)}\alpha) \frac{\mathbf{b}^{(j)}}{|\mathbf{b}^{(j)}|} \right). \end{array} \right. \quad (21)$$

To obtain the global solution of the system (21) in [13], we studied the system before the critical events, and we first considered an associated energy minimizing state,  $(\alpha_\infty^{(k)}, \mathbf{a}_\infty^{(l)})$  of (21). The critical events are the disappearance events, such as, e.g., disappearance of the grains and/or grain boundaries during coarsening of the system, facet interchange and splitting of unstable junctions. Then,  $(\alpha_\infty^{(k)}, \mathbf{a}_\infty^{(l)})$  satisfies,

$$\left\{ \begin{array}{l} \Gamma_\infty^{(j)} \text{ is a line segment between some } \mathbf{a}_\infty^{(l_{j,1})} \text{ and } \mathbf{a}_\infty^{(l_{j,2})}, \\ 0 = -\gamma \sum_{\substack{\text{grain with } \alpha^{(k')} \text{ is the neighbor of the grain with } \alpha^{(k)} \\ \Gamma_\infty^{(j)} \text{ is formed by the two grains with } \alpha^{(k)} \text{ and } \alpha^{(k')}}} |\Gamma_\infty^{(j)}| \sigma_\theta(\alpha_\infty^{(k)} - \alpha_\infty^{(k')}), \\ \mathbf{0} = \eta \sum_{\mathbf{a}_\infty^{(l)} \in \Gamma_\infty^{(j)}} \left( \sigma(\Delta^{(j)}\alpha_\infty) \frac{\mathbf{b}_\infty^{(j)}}{|\mathbf{b}_\infty^{(j)}|} \right). \end{array} \right. \quad (22)$$

Hence, the total energy  $E_\infty$  of the grain boundary network (22) is

$$E_\infty = \sum_j \sigma(\Delta^{(j)}\alpha_\infty) |\mathbf{b}_\infty^{(j)}| = \inf \left\{ \sum_j \sigma(\Delta^{(j)}\alpha) |\mathbf{b}^{(j)}| \right\}. \quad (23)$$

*Remark 4* Note, we assumed in (21)-(22) that the total number of grains, grain boundaries and triple junctions are the same as in the initial configuration (assumption of no critical events in the network).

Further, if there is a neighborhood  $U^{(l)} \subset \mathbb{R}^2$  of  $\mathbf{a}_\infty^{(l)}$  such that

$$E_\infty < \sum_j |\mathbf{b}^{(j)}| \quad (24)$$

for all  $\mathbf{a}^{(l)} \in U^{(l)}$ , one can obtain a priori estimate for the triple junctions, and, hence, obtain the time global solution of (21). Note that, the assumption (24) is related to the boundary condition of the line segments  $\Gamma_t^{(j)}$ . Further, if the energy minimizing

state is unique, then we can proceed with the same argument as in Lemma 4.1 in [13], and obtain the global solution (21) near the energy minimizing state.

*Remark 5* Note that, the solution of (22) may not be unique even though the grain orientations are constant (misorientation is zero) [13].

The asymptotics of the grain boundary networks are rather nontrivial. Our arguments in [13] were based on the uniqueness of the equilibrium state (9). However, we do not know the uniqueness of solutions of the equilibrium state for the grain boundary network (22). Thus, in general we cannot take a full limit for the large time asymptotic behavior of the solution of the network model (21). But, one can show, the following result instead,

**Corollary 2 ([13, Corollary 6.1])** *In a grain boundary network (21), assume that the initial configuration is sufficiently close to an associated energy minimizing state (22). Then, there is a global solution  $(\alpha^{(k)}, \mathbf{a}^{(l)})$  of (21). Furthermore, there exists a time sequence  $t_n \rightarrow \infty$  such that  $(\alpha^{(k)}(t_n), \mathbf{a}^{(l)}(t_n))$  converges to an associated equilibrium configuration (22).*

## 4 Experiments and Numerical Simulations

In this section we present results of some experiments in thin films and numerical study of the grain growth using models of planar grain boundary network from Section 3. The energetics and connectivity of the grain boundary network play a crucial role in determining the properties of a material across multiple scales, see also Sections 2-3. Therefore, our main focus here is to develop a better understanding of the energetic properties of the experimental and computational microstructures.

### 4.1 Experimental Results: Grain Boundary Character Distribution

To more fully characterize a microstructure, it is necessary to consider the types and energies of the constituent grain boundaries, in addition to geometric features such as grain size. Indeed, experiments and simulations over the past 30+ years have led to the discovery and notion of the Grain Boundary Character Distribution (GBCD) [2, 3, 32, 19, 30, 33]. *The GBCD, denoted by  $\rho$ , is an empirical distribution of the relative area (in 3D) or relative length (in 2D) of interface/grain boundaries with a given misorientation and boundary normal.* The GBCD can be viewed as a leading statistical descriptor to characterize the texture of the grain boundary network (see, e.g., [2, 3, 19, 30, 33, 5]).

Figure 3 presents the GBCD for four different misorientations for an as-deposited aluminum film with near random orientation distribution. The details of film deposition, sample preparation and precession electron diffraction crystal orientation

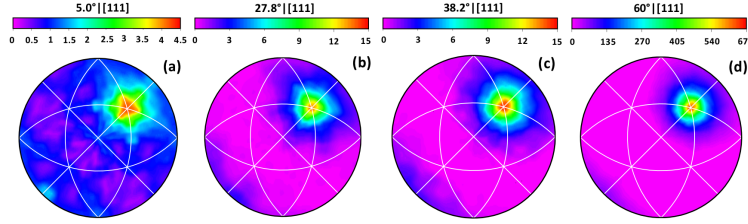


**Fig. 3** Experiments: (a-d) Grain boundary character distribution of 100 nm-thick, as-deposited Al film with a mean grain size of approximately 100 nm for four given misorientations. Misorientations are specified as angle-axis pairs. Pseudosymmetry cleanup of the crystal orientation maps was used in generating the figures. The scale is multiples of random distribution.

mapping in the transmission electron microscope are given in [31]. However, in contrast to [31], the orientation data were subjected to the same cleanup procedure as for the grain size distribution, namely the pseudosymmetry cleanup procedure detailed in [24] with the exception of the  $60^\circ[111]$  boundaries, which are clearly abundant and should not be removed. The minimum grain size of the dilation cleanup step was 20 pixels.

Given that grain boundaries have five crystallographic degrees of freedom - three to specify the misorientation across the grain boundary, and two to define the normal to the boundary, the two-dimensional graphical presentation of the GBCD as in Figure 3 is achieved in the following manner. To begin, a given misorientation is selected, for example,  $5^\circ[111]$ . The rotation axis, here  $[111]$ , is given by the Miller indices of the crystallographic direction that is common to both grains on either side of the boundary. The misorientation angle is usually, but not always, chosen to be within the fundamental zone of misorientations, which for cubic crystals has a minimum of zero and a maximum of  $62.8^\circ$ . Common choices of angles are either those of low angle boundaries, with rotation angles of less than 15 degrees, or those of coincident site lattice (CSL) type. In Figure 3, the selected rotation angles about the  $[111]$  axis of  $27.8^\circ[111]$ ,  $38.2^\circ[111]$  and  $60^\circ[111]$  correspond to CSL designations  $\Sigma 13b$ ,  $\Sigma 7$  and  $\Sigma 3$ , respectively. The numerical value in the  $\Sigma$  designation is the reciprocal of the number of atomic sites that are coincident in the crystallographic plane perpendicular to rotation axis. For face centered cubic crystals, the Miller indices of this plane are the same as the Miller indices of the misorientation axis, e.g., the  $(111)$  plane for the  $[111]$  rotation axis. The letters a or b in the  $\Sigma$  designation then indicate different angle-axis pairs with the same number of coincident sites. Note that the CSL designation does not specify the grain boundary plane that is present in the sample; rather it specifies only a given misorientation.

Next, the grain boundary planes present in the experimental sample for the given misorientation are represented by the crystallographic directions normal to the planes in standard stereographic projections, such as those in Figure 3. The use of stereographic projection rather than other types of projections in single crystal or bicrystal crystallography of materials has been common practice. Its choice is based on the fact that it is an angle-preserving projection that does not depend on the size of

the crystal (from nano to macro). For cubic crystals, the standard projection has the [001] cubic crystal axis pointing out of the page thereby projecting onto the page as the origin of the plot at the center of the (projected equatorial) circle. In Figure 3, the [100] crystallographic axis points to the right, and the [010] crystallographic axis points up, thereby defining a right-handed axis set.

The stereographic projections of the boundary plane normals such as those of Figure 3 then show the abundance of grain boundary plane normals in multiples of random distribution (MRD) on the thermal scale. The MRD is similar to a probability density plot, but its integrated value is 2, rather than 1, since every grain boundary segment is counted twice, once for the grain on one side of the boundary and once for the grain on the other side of the boundary. When the direction normal to the boundary plane and the misorientation axis are the same, the grain boundary is termed a twist boundary, since the axis of rotation is normal to the observed boundary plane. In Figure 3, a high relative intensity is seen at the position of the [111] twist boundaries for all four selected misorientations. If, on the other hand, the high intensities were seen as bands along a great circle ninety degrees away from the chosen misorientation axis, then the boundaries would have been designated as tilt boundaries, with the misorientation axis in the plane of the grain boundary. In effect, GBCD plots such as those of Figure 3 make manifest texture formation in the grain boundary network, see also numerical experiments Section 4.2.

The most striking feature of Figure 3 is the very high abundance of  $60^\circ[111]$  boundaries, which show a population of several hundred times MRD. Given that the majority of the boundary planes were also found to be (111), this sample is said to have a large population of coherent  $\Sigma 3$ , or so-called coherent twin boundaries.  $\Sigma 3$  boundaries constitute approximately one quarter of all the boundaries in this sample. In contrast, for a "bulk" aluminum sample, i.e., in an aluminum sample with mean grain size of  $23\ \mu\text{m}$ , the population of  $\Sigma 3$  boundaries is more than ten times lower [31]. The very high population of  $\Sigma 3$  boundaries in the thin film sample of Figure 3 is likely a result of the structure forming processes that take place during film deposition, rather than a result of normal grain growth. The evolution of the grain boundary network and the GBCD of this sample towards equilibrium or steady-state will be determined by the dynamics of the grain boundaries and the relaxation time scales for the boundary curvature, misorientation and triple junctions, for which models and simulations are presented in the current work. We note that in experimental samples where GBCD has reached steady-state, the GBCD averaged over its five crystallographic parameters is inversely related to the grain boundary energy density similar to the GBCD extracted from grain growth models, Section 4.2. Laboratory-based experimental quantification of grain boundary dynamics via in-situ annealing experiments similar to the experiment in Figure 1, together with intermittent mapping of crystal orientations for determination of the evolving GBCD will be the key to connecting more closely experimental findings to mathematical and computational models of grain growth. These experiments are the subject of the ongoing research.

## 4.2 Numerical Experiments

Here, we present several numerical experiments to illustrate the effects of different time scales, such as the dynamic orientations/misorientations (grains “rotations”) and mobility of the triple junctions, as well as we compare the grain growth model with curvature (20) and model without curvature (21), as described in Sections 2-3.

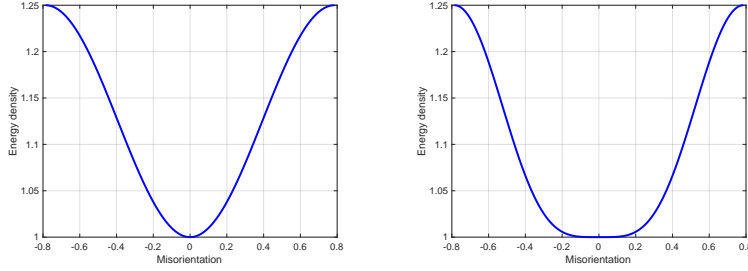


**Fig. 4** Grain boundary energy density function  $\sigma(\Delta\alpha)$ : (a) *Left plot*,  $\sigma = 1 + 0.25 \sin^2(2\Delta\alpha)$  and (b) *Right plot*,  $\sigma = 1 + 0.25 \sin^4(2\Delta\alpha)$ .

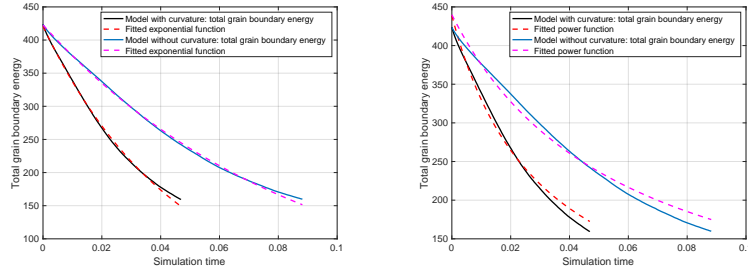


**Fig. 5** One run of 2D trial with 10000 initial grains: (a) *Left plot*, Total grain boundary energy plot, model with curvature (solid black) versus fitted exponential decaying function  $y(t) = 420.9 \exp(-22.13t)$  (dashed red). Total grain boundary energy plot, model without curvature (solid blue) versus fitted exponential decaying function  $y(t) = 422.8 \exp(-11.64t)$  (dashed magenta); (b) *Right plot*, Total grain boundary energy plot, model with curvature (solid black) versus fitted power function  $y_1(t) = 438.8797(1.0 + 32.9489t)^{-1}$  (dashed red). Total grain boundary energy plot, model without curvature (solid blue) versus fitted power function  $y_1(t) = 439.9588(1.0 + 17.1792t)^{-1}$  (dashed magenta). Mobility of the triple junctions is  $\eta = 10$  and the misorientation parameter  $\gamma = 1$ . Grain boundary energy density  $\sigma = 1 + 0.25 \sin^2(2\Delta\alpha)$ .

In particular, the main goal of our numerical experiments is to illustrate the time scales effect of curvature - through grain boundary mobility  $\mu$ , mobility of the triple junctions  $\eta$ , and misorientation parameter  $\gamma$  on how the grain boundary system

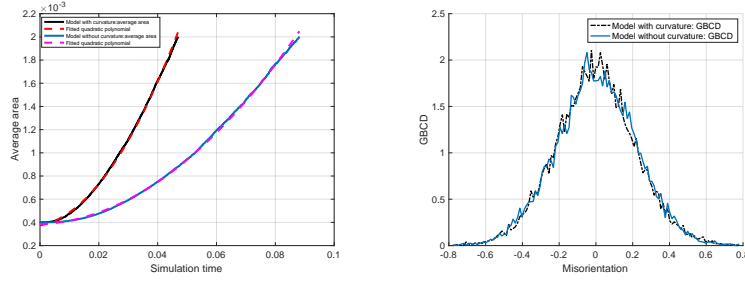


**Fig. 6** (a) *Left plot*, One run of 2D trial with 10000 initial grains: Growth of the average area of the grains, model with curvature (solid black) versus fitted quadratic polynomial function  $y(t) = 0.6575t^2 + 0.004668t + 0.0003745$  (dashed red). Growth of the average area of the grains, model without curvature (solid blue) versus fitted quadratic polynomial function  $y(t) = 0.2025t^2 + 0.001016t + 0.0003844$  (dashed magenta); (b) *Right plot*, GBCD (black curve, model with curvature) and GBCD (blue curve, model without curvature) at  $T_\infty$  averaged over 3 runs of 2D trials with 10000 initial grains. Mobility of the triple junctions is  $\eta = 10$  and the misorientation parameter  $\gamma = 1$ . Grain boundary energy density  $\sigma = 1 + 0.25 \sin^2(2\Delta\alpha)$ .

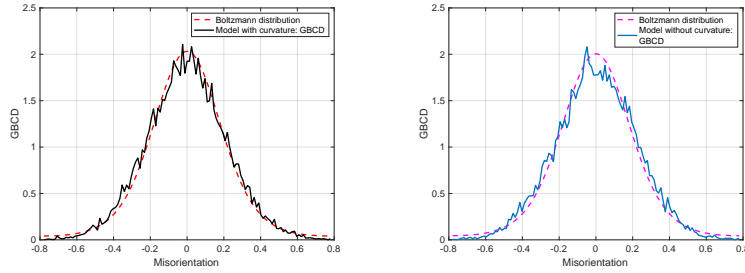


**Fig. 7** (a) *Left plot*, Model with curvature, GBCD (black curve) at  $T_\infty$  averaged over 3 runs of 2D trials with 10000 initial grains versus Boltzmann distribution with “temperature”-  $D \approx 0.0641$  (dashed red curve). (b) *Right plot*, Model without curvature, GBCD (blue curve) at  $T_\infty$  averaged over 3 runs of 2D trials with 10000 initial grains versus Boltzmann distribution with “temperature”-  $D \approx 0.0655$  (dashed magenta curve). Mobility of the triple junctions is  $\eta = 10$  and the misorientation parameter  $\gamma = 1$ . Grain boundary energy density  $\sigma = 1 + 0.25 \sin^2(2\Delta\alpha)$ .

decays energy and coarsens with time. For that we will numerically study evolution of the total grain boundary energy,

$$E(t) = \sum_j \sigma(\Delta^{(j)}\alpha) |\Gamma_t^{(j)}|, \quad (25)$$

where as before,  $\Delta^{(j)}\alpha$  is a misorientation of the grain boundary  $\Gamma_t^{(j)}$ , and  $|\Gamma_t^{(j)}|$  is the length of the grain boundary. We will also consider the growth of the average area, defined as,

$$A(t) = \frac{4}{N(t)}, \quad (26)$$

here 4 is the total area of the sample, and  $N(t)$  is the total number of grains at time  $t$ . The growth of the average area is closely related to the coarsening rate

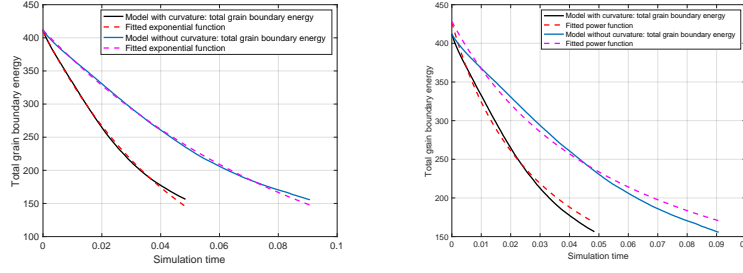


**Fig. 8** One run of 2D trial with 10000 initial grains: (a) *Left plot*, Total grain boundary energy plot, model with curvature (solid black) versus fitted exponential decaying function  $y(t) = 409.8 \exp(-21.38t)$  (dashed red). Total grain boundary energy plot, model without curvature (solid blue) versus fitted exponential decaying function  $y(t) = 411.6 \exp(-11.3t)$  (dashed magenta); (b) *Right plot*, Total grain boundary energy plot, model with curvature (solid black) versus fitted power function  $y_1(t) = 426.9841(1.0 + 31.746t)^{-1}$  (dashed red). Total grain boundary energy plot, model without curvature (solid blue) versus fitted power function  $y_1(t) = 428.2145(1.0 + 16.6556t)^{-1}$  (dashed magenta). Mobility of the triple junctions is  $\eta = 10$  and the misorientation parameter  $\gamma = 1$ . Grain boundary energy density  $\sigma = 1 + 0.25 \sin^4(2\Delta\alpha)$ .

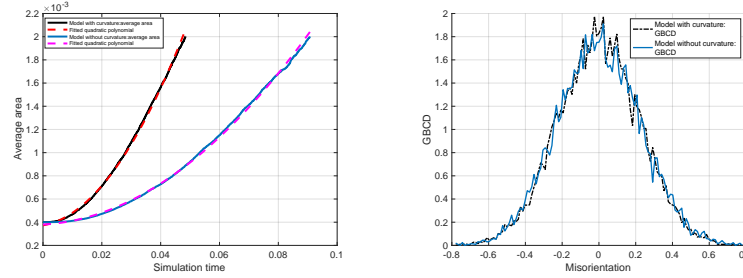


**Fig. 9** (a) *Left plot*, One run of 2D trial with 10000 initial grains: Growth of the average area of the grains, model with curvature (solid black) versus fitted quadratic polynomial function  $y(t) = 0.6258t^2 + 0.004538t + 0.0003732$  (dashed red). Growth of the average area of the grains, model without curvature (solid blue) versus fitted quadratic polynomial function  $y(t) = 0.1866t^2 + 0.001377t + 0.0003799$  (dashed magenta); (b) *Right plot*, GBCD (black curve, model with curvature) and GBCD (blue curve, model without curvature) at  $T_\infty$  averaged over 3 runs of 2D trials with 10000 initial grains. Mobility of the triple junctions is  $\eta = 10$  and the misorientation parameter  $\gamma = 1$ . Grain boundary energy density  $\sigma = 1 + 0.25 \sin^4(2\Delta\alpha)$ .

of the grain system that undergoes critical/disappearance events. However, it is important to note that critical events include not only grain disappearance, but also facet/grain boundary disappearance, facet interchange, and splitting of unstable junctions, for more details about numerical modeling of critical events in 2D, see e.g. [21, 8]. Further, we will investigate the distribution of the grain boundary character distribution (GBCD)  $\rho(\Delta^{(j)}\alpha)$  at a final time of the simulations  $T_\infty$  (defined below) under a simplified assumption on a grain boundary energy density, namely that  $\sigma(\Delta^{(j)}\alpha)$  is only a function of the misorientation, see also Sections 2-3. The GBCD (in this context) is an empirical statistical measure of the relative length (in 2D) of the grain boundary interface with a given lattice misorientation,

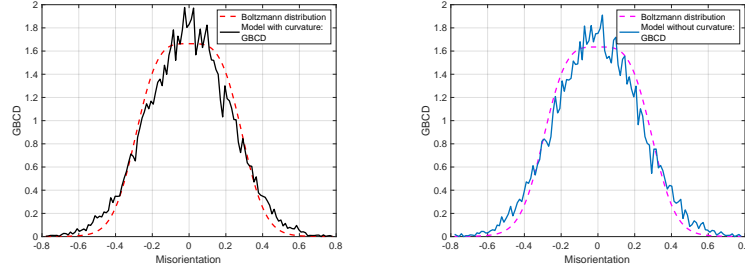


**Fig. 10** (a) *Left plot*, Model with curvature, GBCD (black curve) at  $T_\infty$  averaged over 3 runs of 2D trials with 10000 initial grains versus Boltzmann distribution with “temperature”-  $D \approx 0.035$  (dashed red curve). (b) *Right plot*, Model without curvature, GBCD (blue curve) at  $T_\infty$  averaged over 3 runs of 2D trials with 10000 initial grains versus Boltzmann distribution with “temperature”-  $D \approx 0.035$  (dashed magenta curve). Mobility of the triple junctions is  $\eta = 10$  and the misorientation parameter  $\gamma = 1$ . Grain boundary energy density  $\sigma = 1 + 0.25 \sin^4(2\Delta\alpha)$ .

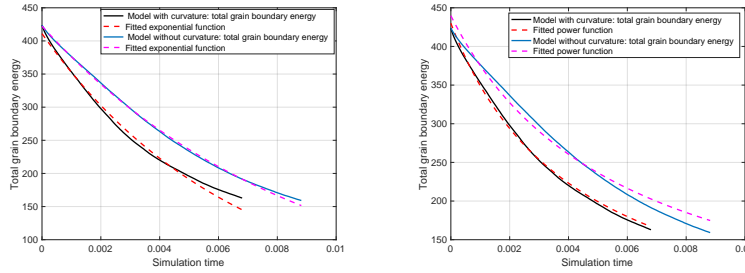


**Fig. 11** One run of 2D trial with 10000 initial grains: (a) *Left plot*, Total grain boundary energy plot, model with curvature (solid black) versus fitted exponential decaying function  $y(t) = 411 \exp(-153t)$  (dashed red). Total grain boundary energy plot, model without curvature (solid blue) versus fitted exponential decaying function  $y(t) = 422.4 \exp(-116.3t)$  (dashed magenta); (b) *Right plot*, Total grain boundary energy plot, model with curvature (solid black) versus fitted power function  $y_1(t) = 430.0278(1.0 + 231.6960t)^{-1}$  (dashed red). Total grain boundary energy plot, model without curvature (solid blue) versus fitted power function  $y_1(t) = 439.8212(1.0 + 171.9395t)^{-1}$  (dashed magenta). Mobility of the triple junctions is  $\eta = 100$  and the misorientation parameter  $\gamma = 1$ . Grain boundary energy density  $\sigma = 1 + 0.25 \sin^2(2\Delta\alpha)$ .

$$\rho(\Delta^{(j)}\alpha, t) = \text{relative length of interface of lattice misorientation } \Delta^{(j)}\alpha \text{ at time } t, \\ \text{normalized so that } \int_{\Omega_{\Delta^{(j)}\alpha}} \rho d\Delta^{(j)}\alpha = 1, \quad (27)$$

where we consider  $\Omega_{\Delta^{(j)}\alpha} = [-\frac{\pi}{4}, \frac{\pi}{4}]$  in the numerical experiments below (for planar grain boundary network, it is reasonable to consider such range for the misorientations). For more details, see for example [5, 13]. In all our tests below, we compare the GBCD at  $T_\infty$  to the stationary solution of the Fokker-Planck equation, the Boltzmann distribution for the grain boundary energy density  $\sigma(\Delta^{(j)}\alpha)$ ,



$$\rho_D(\Delta^{(j)}\alpha) = \frac{1}{Z_D} e^{-\frac{\sigma(\Delta^{(j)}\alpha)}{D}},$$

with partition function, i.e., normalization factor

$$Z_D = \int_{\Omega_{\Delta^{(j)}\alpha}} e^{-\frac{\sigma(\Delta^{(j)}\alpha)}{D}} d\Delta^{(j)}\alpha, \quad (28)$$

[6, 5, 8, 4]. We employ the Kullback-Leibler relative entropy test to obtain a unique “temperature-like” parameter  $D$  and to construct the corresponding Boltzmann distribution for the GBCD at  $T_\infty$  as it was originally done in [6, 5, 8, 4]. Note, as we also discussed in Section 4.1, GBCD is a primary candidate to characterize texture of the grain boundary network, and is inversely related to the grain boundary energy density as discovered in experiments and simulations. The reader can consult, for example, [6, 5, 8, 4] for more details about GBCD and the theory of the GBCD. In the numerical experiments in this paper, we consider two choices for the grain boundary energy density as plotted in Figure 4 and given below,

$$\sigma(\Delta^{(j)}\alpha) = 1 + 0.25 \sin^2(2\Delta^{(j)}\alpha) \text{ and } \sigma(\Delta^{(j)}\alpha) = 1 + 0.25 \sin^4(2\Delta^{(j)}\alpha).$$

We consider simulation of 2D grain boundary network using the algorithm based on the sharp interface approach [13] with dynamic misorientation and finite mobility of the triple junctions which we also extended to a model without curvature (21). Note, that the algorithm [13] is a further extension of the algorithm from [8, 4]. We recall that in the numerical scheme we work with a variational principle. The cornerstone of the algorithm, which assures its stability, is the discrete dissipation inequality for the total grain boundary energy that holds when either the discrete Herring boundary condition ( $\eta \rightarrow \infty$ ) or discrete “dynamic boundary condition” (finite mobility  $\eta$  of the triple junctions, third equation of (20) or of (21)) is satisfied at the triple junctions. We also recall that in the numerical algorithm for model (20) we impose the Mullins’ theory (first equation of (20)) as the local evolution law for the grain boundaries (and the time scale  $\mu$  is kept finite). For model (21),  $\mu \rightarrow \infty$ , hence the dynamics of the grain boundaries are defined by the evolution of the triple junctions (the third equation of (21)) and by the grains rotation (the second equation of (21)). The reader can consult [8, 4, 13] for more details about numerical algorithm based on the sharp interface approach.

In all the numerical tests below we initialized our system with  $10^4$  cells/grains with normally distributed misorientation angles at initial time  $t = 0$ . We also assume that the final time of the simulations  $T_\infty$  is the time when approximately 80% of grains disappeared from the system, namely the time when only about 2000 cells/grains remain. The final time is selected based on the system (20) with no dynamic misorientations ( $\gamma = 0$ ) and with the Herring condition at the triple junctions ( $\eta \rightarrow \infty$ ) and, it is selected to ensure that statistically significant number of grains still remain in the system and that the system reached its statistical steady-state. Therefore, all the numerical results which are presented below are for the grain boundary system that undergoes critical/disappearance events.

First, we study the effect of dynamics of triple junctions on the dissipation and coarsening of the system, see Figures 5-22 (we consider different values of misorientation parameter  $\gamma$  for these tests). We observe that for smaller values of the mobility of the triple junctions  $\eta$ , the energy decay  $E(t)$  is well-approximated by an exponential function for both models, for the model with curvature (20) and for the model without curvature (21), see Figures 5 and 8 (left plots). This is consistent with the results of our theory, see Sections 2-3 and [14, 13], even though, the theoretical results are obtained under assumption of no critical events and  $\mu \rightarrow \infty$  (for grain growth model without curvature). This result indicates that for lower mobility of the triple junctions  $\eta$ , the dynamics of triple junctions have a dominant effect on the grain growth, see model (21). This explains the similarity in the energy decay for grain growth model with curvature (20) and without curvature (21) when  $\eta = 10$ , Figures 5 and 8. In comparison, we also present fit to a power law decaying function, see Figures 5 and 8 (right plots). The power law function does not seem to give as good approximation in this case.

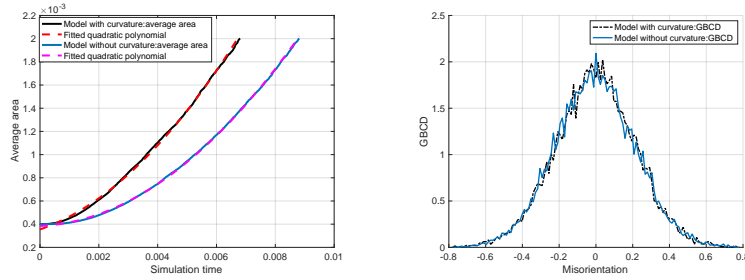


**Fig. 12** (a) *Left plot*, One run of 2D trial with 10000 initial grains: Growth of the average area of the grains, model with curvature (solid black) versus fitted quadratic polynomial function  $y(t) = 23.47t^2 + 0.08748t + 0.0003549$  (dashed red). Growth of the average area of the grains, model without curvature (solid blue) versus fitted quadratic polynomial function  $y(t) = 19.74t^2 + 0.01157t + 0.0003843$  (dashed magenta); (b) *Right plot*, GBCD (black curve, model with curvature) and GBCD (blue curve, model without curvature) at  $T_\infty$  averaged over 3 runs of 2D trials with 10000 initial grains. Mobility of the triple junctions is  $\eta = 100$  and the misorientation parameter  $\gamma = 1$ . Grain boundary energy density  $\sigma = 1 + 0.25 \sin^2(2\Delta\alpha)$ .

However, for a larger value of  $\eta = 100$ , Figures 11, 14, 17 and 20, we obtain that the total grain boundary energy does not follow exponential decay anymore for the model with curvature (20), but rather the energy decay is closer to a power law. Thus, the curvature time scale-the grain boundary evolution has a dominant effect for large  $\eta$ . However, for the model without curvature (21), the energy decay is still well approximated by the exponential function which is consistent with the theory, Sections 2-3. Note also, that the numerically observed energy decay rates increase with the mobility  $\eta$  of the triple junctions which is also consistent with the developed theory [13]. In addition, we observe that the average area grows as a quadratic function in time for the finite mobility  $\eta$  of the triple junctions, Figures 6, 9, 12, 15, 18 and 21 (left plots) and see also our earlier work [13]. We also observe that the coarsening rate of grain growth slows down with the smaller  $\eta$ . In addition,

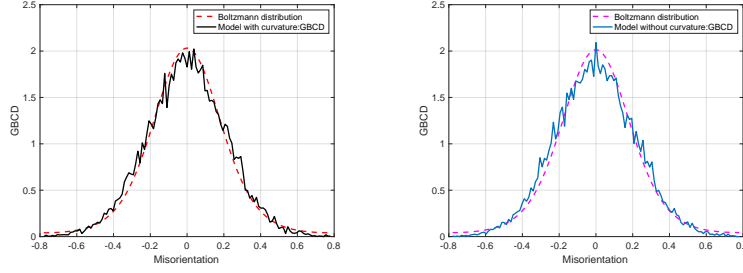


**Fig. 13** (a) *Left plot*, Model with curvature, GBCD (black curve) at  $T_\infty$  averaged over 3 runs of 2D trials with 10000 initial grains versus Boltzmann distribution with “temperature”-  $D \approx 0.0641$  (dashed red curve). (b) *Right plot*, Model without curvature, GBCD (blue curve) at  $T_\infty$  averaged over 3 runs of 2D trials with 10000 initial grains versus Boltzmann distribution with “temperature”-  $D \approx 0.0651$  (dashed magenta curve). Mobility of the triple junctions is  $\eta = 100$  and the misorientation parameter  $\gamma = 1$ . Grain boundary energy density  $\sigma = 1 + 0.25 \sin^2(2\Delta\alpha)$ .

we note that the energy decay in our numerical tests is consistent with the growth of the average area. Moreover, we observe that neither dynamics of the triple junctions nor curvature show as much of an effect on the GBCD, see Figures 6 (right plot)-7, 9 (right plot)-10, 12 (right plot)-13, 15 (right plot)-16, 18 (right plot)-19 and 21 (right plot)-22 (note, the “temperature” like parameter  $D$  also accounts for various critical events—grains disappearance, facet/grain boundary disappearance, facet interchange, splitting of unstable junctions. It will be part of our future study to understand how  $D$  depends on the critical events.)

For the other series of tests, we vary the misorientation parameter  $\gamma$ , second equation of (20) or of (21) (and we set the mobility of the triple junctions  $\eta = 100$ , third equation of (20) or of (21)). We do not observe as much of an effect on the energy decay or average area growth in this case, but we observe the significant effect on the GBCD and the diffusion coefficient/“temperature”-like parameter  $D$ , see Figures 5-16 (with the misorientation parameter  $\gamma = 1$ ) and Figures 17-22 (with larger values of the misorientation parameter  $\gamma$ ). As concluded from our numerical results, larger values of  $\gamma$  give smaller diffusion coefficient/“temperature”-like parameter  $D$ , and hence higher GBCD peak near misorientation 0. This is consistent with our theory that basically, larger misorientation parameter  $\gamma$  produces direct motion of misorientations towards equilibrium state of zero misorientations, see Section 2 and also [13]. Furthermore, from all of our numerical experiments with dynamic misorientations and with different triple junction mobilities, we observe that the GBCD at time  $T_\infty$  is well-approximated by the Boltzmann distribution for the grain boundary energy density see Figures 7, 10, 13, 16, 19 and 22, as well as consistent with experimental findings as discussed in Section 4.1, which is similar to the work in [6, 5, 8, 4], but more detailed analysis needs to be done for a system that undergoes critical events to understand the relation between GBCD, “temperature”-like/diffusion parameter  $D$ , and different relaxation time scales, as well as the effect of the time scales on the dissipation mechanism and certain coarsening rates.

**Remark 6** Note that, we performed 3 runs for each numerical test presented in this work. We report results of a single run for the energy decay and growth of the average area (the results from the other two runs for each test were very similar to the presented ones), and we illustrate averaged over the 3 runs the GBCD statistics. The curve-fitting for the energy and the average area plots was done using Matlab ([27]) toolbox cftool.

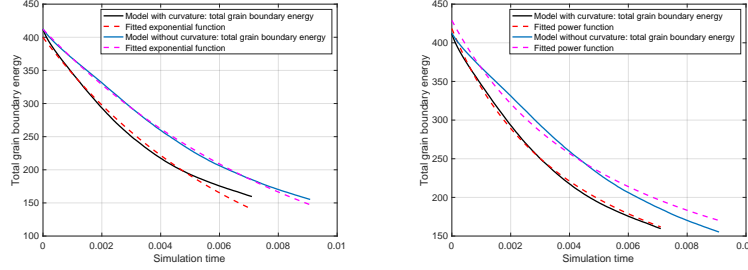


**Fig. 14** One run of 2D trial with 10000 initial grains: (a) *Left plot*, Total grain boundary energy plot, model with curvature (solid black) versus fitted exponential decaying function  $y(t) = 399.7 \exp(-147.2t)$  (dashed red). Total grain boundary energy plot, model without curvature (solid blue) versus fitted exponential decaying function  $y(t) = 412.1 \exp(-113.3t)$  (dashed magenta); (b) *Right plot*, Total grain boundary energy plot, model with curvature (solid black) versus fitted power function  $y_1(t) = 418.3970(1.0 + 223.2641t)^{-1}$  (dashed red). Total grain boundary energy plot, model without curvature (solid blue) versus fitted power function  $y_1(t) = 428.9782(1.0 + 167.5042t)^{-1}$  (dashed magenta). Mobility of the triple junctions is  $\eta = 100$  and the misorientation parameter  $\gamma = 1$ . Grain boundary energy density  $\sigma = 1 + 0.25 \sin^4(2\Delta\alpha)$ .

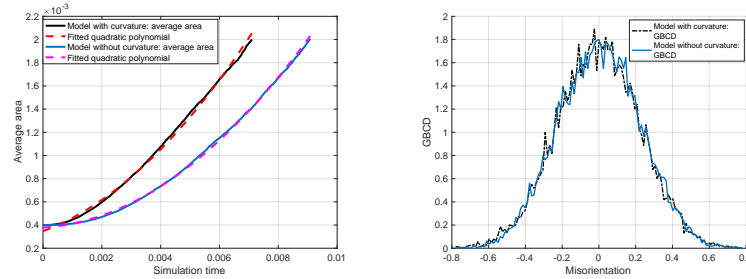


**Fig. 15** (a) *Left plot*, One run of 2D trial with 10000 initial grains: Growth of the average area of the grains, model with curvature (solid black) versus fitted quadratic polynomial function  $y(t) = 20.63t^2 + 0.09393t + 0.0003472$  (dashed red). Growth of the average area of the grains, model without curvature (solid blue) versus fitted quadratic polynomial function  $y(t) = 18.31t^2 + 0.01553t + 0.0003786$  (dashed magenta); (b) *Right plot*, GBCD (black curve, model with curvature) and GBCD (blue curve, model without curvature) at  $T_\infty$  averaged over 3 runs of 2D trials with 10000 initial grains. Mobility of the triple junctions is  $\eta = 100$  and the misorientation parameter  $\gamma = 1$ . Grain boundary energy density  $\sigma = 1 + 0.25 \sin^4(2\Delta\alpha)$ .

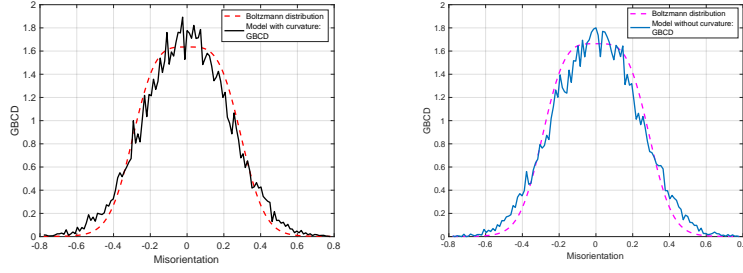


**Fig. 16** (a) *Left plot*, Model with curvature, GBCD (black curve) at  $T_\infty$  averaged over 3 runs of 2D trials with 10000 initial grains versus Boltzmann distribution with “temperature”-  $D \approx 0.037$  (dashed red curve). (b) *Right plot*, Model without curvature, GBCD (blue curve) at  $T_\infty$  averaged over 3 runs of 2D trials with 10000 initial grains versus Boltzmann distribution with “temperature”-  $D \approx 0.035$  (dashed magenta curve). Mobility of the triple junctions is  $\eta = 100$  and the misorientation parameter  $\gamma = 1$ . Grain boundary energy density  $\sigma = 1 + 0.25 \sin^4(2\Delta\alpha)$ .

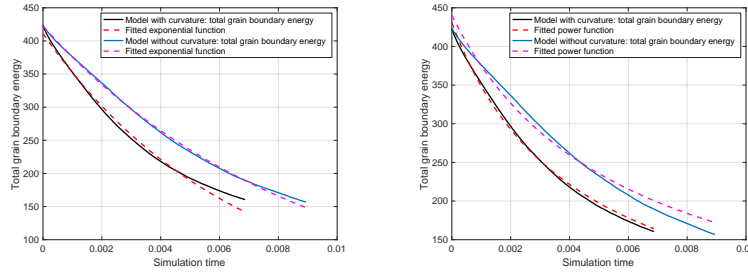


**Fig. 17** One run of 2D trial with 10000 initial grains: (a) *Left plot*, Total grain boundary energy plot, model with curvature (solid black) versus fitted exponential decaying function  $y(t) = 411.2 \exp(-154.9t)$  (dashed red). Total grain boundary energy plot, model without curvature (solid blue) versus fitted exponential decaying function  $y(t) = 422.2 \exp(-116.8t)$  (dashed magenta); (b) *Right plot*, Total grain boundary energy plot, model with curvature (solid black) versus fitted power function  $y_1(t) = 430.8310(1.0 + 236.0718t)^{-1}$  (dashed red). Total grain boundary energy plot, model without curvature (solid blue) versus fitted power function  $y_1(t) = 440.1947(1.0 + 173.8526t)^{-1}$  (dashed magenta). Mobility of the triple junctions is  $\eta = 100$ , the misorientation parameter  $\gamma = 250$  (curvature model) and  $\gamma = 300$  (vertex model). Grain boundary energy density  $\sigma = 1 + 0.25 \sin^2(2\Delta\alpha)$ .

## Conclusion

In this work, we conducted extensive numerical studies of the two models developed in [14, 13]: a model with curved grain boundaries and a model without curvature/“vertex model” of planar grain boundaries network with the dynamic lattice misorientations and with the drag of triple junctions. The goal of our study was to further understand the effect of relaxation time scales, e.g. of the curvature of grain boundaries, mobility of triple junctions, and dynamics of misorientations on how the grain boundary system decays energy and coarsens with time. We also presented and discussed relevant experimental results of grain growth in thin films.

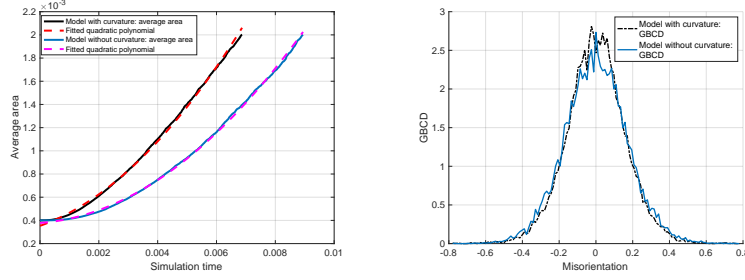


**Fig. 18** (a) *Left plot*, One run of 2D trial with 10000 initial grains: Growth of the average area of the grains, model with curvature (solid black) versus fitted quadratic polynomial function  $y(t) = 23.18t^2 + 0.08941t + 0.0003532$  (dashed red). Growth of the average area of the grains, model without curvature (solid blue) versus fitted quadratic polynomial function  $y(t) = 18.56t^2 + 0.01824t + 0.000378$  (dashed magenta); (b) *Right plot*, GBCD (black curve, model with curvature) and GBCD (blue curve, model without curvature) at  $T_\infty$  averaged over 3 runs of 2D trials with 10000 initial grains. Mobility of the triple junctions is  $\eta = 100$ , the misorientation parameter  $\gamma = 250$  (curvature model) and  $\gamma = 300$  (vertex model). Grain boundary energy density  $\sigma = 1 + 0.25 \sin^2(2\Delta\alpha)$ .

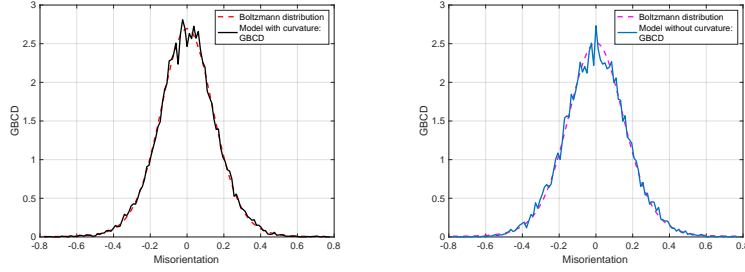


**Fig. 19** (a) *Left plot*, Model with curvature, GBCD (black curve) at  $T_\infty$  averaged over 3 runs of 2D trials with 10000 initial grains versus Boltzmann distribution with “temperature”-  $D \approx 0.0397$  (dashed red curve). (b) *Right plot*, Model without curvature, GBCD (blue curve) at  $T_\infty$  averaged over 3 runs of 2D trials with 10000 initial grains versus Boltzmann distribution with “temperature”-  $D \approx 0.0448$  (dashed magenta curve). Mobility of the triple junctions is  $\eta = 100$ , the misorientation parameter  $\gamma = 250$  (model with curvature) and  $\gamma = 300$  (model without curvature). Grain boundary energy density  $\sigma = 1 + 0.25 \sin^2(2\Delta\alpha)$ .

## Acknowledgments

The authors are grateful to David Kinderlehrer for the fruitful discussions, inspiration and motivation of the work. Matthew Patrick and Amirali Zangiabadi are thanked for assistance with the experimental work. Katayun Barmak acknowledges partial support of NSF DMS-1905492, Yekaterina Epshteyn acknowledges partial support of NSF DMS-1905463, Chun Liu acknowledges partial support of NSF DMS-1759535 and of NSF DMS-1950868, and Masashi Mizuno acknowledges partial support of JSPS KAKENHI Grant No. 18K13446.

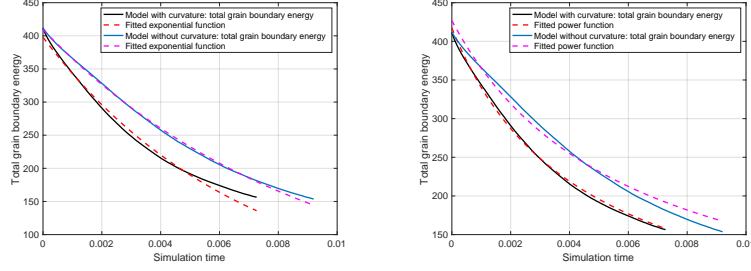


**Fig. 20** One run of 2D trial with 10000 initial grains: (a) *Left plot*, Total grain boundary energy plot, model with curvature (solid black) versus fitted exponential decaying function  $y(t) = 397.8 \exp(-147.8t)$  (dashed red). Total grain boundary energy plot, model without curvature (solid blue) versus fitted exponential decaying function  $y(t) = 409.5 \exp(-113.2t)$  (dashed magenta); (b) *Right plot*, Total grain boundary energy plot, model with curvature (solid black) versus fitted power function  $y_1(t) = 417.4031(1.0 + 226.6032t)^{-1}$  (dashed red). Total grain boundary energy plot, model without curvature (solid blue) versus fitted power function  $y_1(t) = 427.0061(1.0 + 168.5772t)^{-1}$  (dashed magenta) Mobility of the triple junctions is  $\eta = 100$ , the misorientation parameter  $\gamma = 1000$  (curvature model) and  $\gamma = 1500$  (vertex model). Grain boundary energy density  $\sigma = 1 + 0.25 \sin^4(2\Delta\alpha)$ .

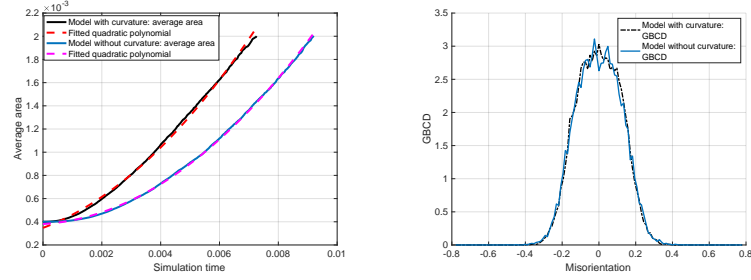


**Fig. 21** (a) *Left plot*, One run of 2D trial with 10000 initial grains: Growth of the average area of the grains, model with curvature (solid black) versus fitted quadratic polynomial function  $y(t) = 19.81t^2 + 0.09408t + 0.0003476$  (dashed red). Growth of the average area of the grains, model without curvature (solid blue) versus fitted quadratic polynomial function  $y(t) = 17.81t^2 + 0.01484t + 0.0003807$  (dashed magenta); (b) *Right plot*, GBCD (black curve, model with curvature) and GBCD (blue curve, model without curvature) at  $T_\infty$  averaged over 3 runs of 2D trials with 10000 initial grains. Mobility of triple junctions is  $\eta = 100$ , the misorientation parameter  $\gamma = 1000$  (curvature model) and  $\gamma = 1500$  (vertex model). Grain boundary energy density  $\sigma = 1 + 0.25 \sin^4(2\Delta\alpha)$ .

## References

1. Helmut Abels, Harald Garcke, and Lars Müller. Stability of spherical caps under the volume-preserving mean curvature flow with line tension. *Nonlinear Anal.*, 117:8–37, 2015.
2. BL Adams, D Kinderlehrer, WW Mullins, AD Rollett, and S Ta'asan. Extracting the relative grain boundary free energy and mobility functions from the geometry of microstructures. *Scripta Materiala*, 38(4):531–536, Jan 13 1998.
3. B.L. Adams, S. Ta'Asan, D. Kinderlehrer, I. Livshits, D.E. Mason, Chun-Te Wu, W.W. Mullins, G.S. Rohrer, A.D. Rollett, and D.M. Saylor. Extracting grain boundary and surface energy from measurement of triple junction geometry. *Interface Science*, 7(3):321–337, Nov 1999.

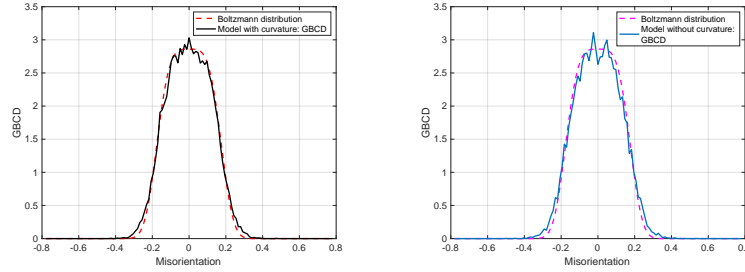


**Fig. 22** (a) *Left plot*, Model with curvature, GBCD (black curve) at  $T_\infty$  averaged over 3 runs of 2D trials with 10000 initial grains versus Boltzmann distribution with “temperature”-  $D \approx 0.005$  (dashed red curve). (b) *Right plot*, Model without curvature, GBCD (blue curve) at  $T_\infty$  averaged over 3 runs of 2D trials with 10000 initial grains versus Boltzmann distribution with “temperature”-  $D \approx 0.005$  (dashed magenta curve). Mobility of the triple junctions is  $\eta = 100$ , the misorientation parameter  $\gamma = 1000$  (model with curvature) and  $\gamma = 1500$  (model without curvature). Grain boundary energy density  $\sigma = 1 + 0.25 \sin^4(2\Delta\alpha)$ .

4. Patrick Bardsley, Katayun Barmak, Eva Eggeling, Yekaterina Epshteyn, David Kinderlehrer, and Shlomo Ta’asan. Towards a gradient flow for microstructure. *Atti Accad. Naz. Lincei Rend. Lincei Mat. Appl.*, 28(4):777–805, 2017.
5. K. Barmak, E. Eggeling, M. Emelianenko, Y. Epshteyn, D. Kinderlehrer, R. Sharp, and S. Ta’asan. Critical events, entropy, and the grain boundary character distribution. *Phys. Rev. B*, 83:134117, Apr 2011.
6. K. Barmak, E. Eggeling, M. Emelianenko, Y. Epshteyn, D. Kinderlehrer, and S. Ta’asan. Geometric growth and character development in large metastable networks. *Rend. Mat. Appl.* (7), 29(1):65–81, 2009.
7. K. Barmak, E. Eggeling, D. Kinderlehrer, R. Sharp, S. Ta’asan, A.D. Rollett, and K.R. Coffey. Grain growth and the puzzle of its stagnation in thin films: The curious tale of a tail and an ear. *Progress in Materials Science*, 58(7):987–1055, 2013.
8. Katayun Barmak, Eva Eggeling, Maria Emelianenko, Yekaterina Epshteyn, David Kinderlehrer, Richard Sharp, and Shlomo Ta’asan. An entropy based theory of the grain boundary character distribution. *Discrete Contin. Dyn. Syst.*, 30(2):427–454, 2011.
9. Kenneth A. Brakke. *The motion of a surface by its mean curvature*, volume 20 of *Mathematical Notes*. Princeton University Press, Princeton, N.J., 1978.
10. Lia Bronsard and Fernando Reitich. On three-phase boundary motion and the singular limit of a vector-valued Ginzburg-Landau equation. *Arch. Rational Mech. Anal.*, 124(4):355–379, 1993.
11. Yun Gang Chen, Yoshikazu Giga, and Shun’ichi Goto. Uniqueness and existence of viscosity solutions of generalized mean curvature flow equations. *J. Differential Geom.*, 33(3):749–786, 1991.
12. Klaus Ecker. *Regularity theory for mean curvature flow*. Progress in Nonlinear Differential Equations and their Applications, 57. Birkhäuser Boston, Inc., Boston, MA, 2004.
13. Yekaterina Epshteyn, Chun Liu, and Masashi Mizuno. Large time asymptotic behavior of grain boundaries motion with dynamic lattice misorientations and with triple junctions drag. 2021. to appear in *Commun. Math. Sci.*, <https://arxiv.org/abs/1910.08022>.
14. Yekaterina Epshteyn, Chun Liu, and Masashi Mizuno. Motion of grain boundaries with dynamic lattice misorientations and with triple junctions drag. *SIAM Journal on Mathematical Analysis*, 53(3):3072–3097, 2021.
15. L. C. Evans and J. Spruck. Motion of level sets by mean curvature. I. *J. Differential Geom.*, 33(3):635–681, 1991.
16. Harald Garcke, Yoshihito Kohsaka, and Daniel Ševčovič. Nonlinear stability of stationary solutions for curvature flow with triple function. *Hokkaido Math. J.*, 38(4):721–769, 2009.



17. Conyers Herring. *Surface Tension as a Motivation for Sintering*, pages 33–69. Springer Berlin Heidelberg, Berlin, Heidelberg, 1999.
18. Lami Kim and Yoshihiro Tonegawa. On the mean curvature flow of grain boundaries. *Ann. Inst. Fourier (Grenoble)*, 67(1):43–142, 2017.
19. D Kinderlehrer, I Livshits, GS Rohrer, S Ta’asan, and P Yu. Mesoscale simulation of the evolution of the grain boundary character distribution. *Recrystallization and grain growth, pts 1 and 2*, 467–470(Part 1-2):1063–1068, 2004.
20. David Kinderlehrer and Chun Liu. Evolution of grain boundaries. *Math. Models Methods Appl. Sci.*, 11(4):713–729, 2001.
21. David Kinderlehrer, Irene Livshits, and Shlomo Ta’asan. A variational approach to modeling and simulation of grain growth. *SIAM J. Sci. Comput.*, 28(5):1694–1715, 2006.
22. Robert V Kohn. Irreversibility and the statistics of grain boundaries. *Physics*, 4:33, 2011.
23. Tim Laux and Felix Otto. Convergence of the thresholding scheme for multi-phase mean-curvature flow. *Calc. Var. Partial Differential Equations*, 55(5):Art. 129, 74, 2016.
24. Xuan Liu, Andrew P. Warren, Noel T. Nuhfer, Anthony D. Rollett, Kevin R. Coffey, and Katayun Barmak. Comparison of crystal orientation mapping-based and image-based measurement of grain size and grain size distribution in a thin aluminum film. *Acta Materialia*, 79:138–145, 2014.
25. Carlo Mantegazza. *Lecture notes on mean curvature flow*, volume 290 of *Progress in Mathematics*. Birkhäuser/Springer Basel AG, Basel, 2011.
26. Carlo Mantegazza, Matteo Novaga, and Vincenzo Maria Tortorelli. Motion by curvature of planar networks. *Ann. Sc. Norm. Super. Pisa Cl. Sci. (5)*, 3(2):235–324, 2004.
27. Matlab MathWorks Inc. Matlab. version 9.4.0 (r2018a). *The MathWorks Inc., Natick, Massachusetts*, 2018.
28. W. W. Mullins. Two-dimensional motion of idealized grain boundaries. *Journal of Applied Physics*, 27(8):900–904, 1956.
29. W. W. Mullins. Theory of thermal grooving. *Journal of Applied Physics*, 28(3):333–339, 1957.
30. Gregory S. Rohrer. Influence of Interface Anisotropy on Grain Growth and Coarsening. *Annu. Rev. Mater. Res.*, 35:99–126, 2005.
31. Gregory S. Rohrer, Xuan Liu, Jiaying Liu, Amith Darbal, Xiwen Chen, Michael A. Berkson, Noel T. Nuhfer, Kevin R. Coffey, and Katayun Barmak. The Grain boundary Character Distribution of a Highly Twinned Nanocrystalline Aluminum Thin Film Compared to Bulk Microcrystalline Aluminum. *J. Mater. Sci.*, 52:9819–9833, 2017.
32. Gregory S. Rohrer, David M. Saylor, Bassem El Dasher, Brent L. Adams, Anthony D. Rollett, and Paul Wynblatt. The distribution of internal interfaces in polycrystals. *Z. Metallkd.*, 95:1–18, 2004.
33. Anthony D. Rollett, S.-B. Lee, R. Campman, and G. S. Rohrer. Three-dimensional characterization of microstructure by electron back-scatter diffraction. *Annual Review of Materials Research*, 37:627–658, 2007.
34. Spencer L. Thomas, Chaozhen Wei, Jian Han, Yang Xiang, and David J. Srolovitz. Disconnection description of triple-junction motion. *Proceedings of the National Academy of Sciences*, 116(18):8756–8765, 2019.
35. C. E. Torres, M. Emelianenko, D. Golovaty, D. Kinderlehrer, and S. Ta’asan. Numerical analysis of the vertex models for simulating grain boundary networks. *SIAM Journal on Applied Mathematics*, 75(2):762–786, 2015.
36. M Upmanyu, D.J Srolovitz, L.S Shvindlerman, and G Gottstein. Molecular dynamics simulation of triple junction migration. *Acta Materialia*, 50(6):1405–1420, 2002.
37. Moneesh Upmanyu, D. J. Srolovitz, L. S. Shvindlerman, and G. Gottstein. Triple junction mobility: A molecular dynamics study. *Interface Science*, 7(3):307–319, Nov 1999.
38. Luchan Zhang, Jian Han, Yang Xiang, and David J. Srolovitz. Equation of motion for a grain boundary. *Phys. Rev. Lett.*, 119:246101, Dec 2017.
39. Luchan Zhang and Yang Xiang. Motion of grain boundaries incorporating dislocation structure. *Journal of the Mechanics and Physics of Solids*, 117:157–178, 2018.